Delft University of Technology

Document Version
Final published version

Licence
CC BY

Citation (APA)
Sagar, S., Sluiter, M. H. F., & Dey, P. (2024). First - Principles study of hydrogen - Carbide interaction in bcc Fe. *International Journal of Hydrogen Energy*, *50*, 211-223. https://doi.org/10.1016/j.ijhydene.2023.09.222

Important note
To cite this publication, please use the final published version (if applicable).
Please check the document version above.

Copyright
In case the licence states "Dutch Copyright Act (Article 25fa)", this publication was made available Green Open Access via the TU Delft Institutional Repository pursuant to Dutch Copyright Act (Article 25fa, the Taverne amendment). This provision does not affect copyright ownership.
Unless copyright is transferred by contract or statute, it remains with the copyright holder.

Sharing and reuse
Other than for strictly personal use, it is not permitted to download, forward or distribute the text or part of it, without the consent of the author(s) and/or copyright holder(s), unless the work is under an open content license such as Creative Commons.

Takedown policy
Please contact us and provide details if you believe this document breaches copyrights.
We will remove access to the work immediately and investigate your claim.

This work is downloaded from Delft University of Technology.

Available online at www.sciencedirect.com

ScienceDirect

journal homepage: www.elsevier.com/locate/he

First - Principles study of hydrogen - Carbide interaction in bcc Fe

Saurabh Sagar, Marcel H.F. Sluiter, Poulumi Dey *

Department of Materials Science and Engineering, Faculty of Mechanical, Maritime and Materials Engineering, Delft University of Technology, Mekelweg 2, 2628CD, Delft, the Netherlands

HIGHLIGHTS

- DFT investigation of effectiveness of TiC, VC and NbC as hydrogen traps in bcc Fe.
- Preferential segregation of hydrogen in the bulk or at the interface.
- Hydrogen migration barrier in bulk carbides and at the coherent interface.
- Novel insights into vacancy and hydrogen-vacancy complex formation.

ARTICLE INFO

Article history:
Received 25 July 2023
Received in revised form
18 September 2023
Accepted 20 September 2023
Available online 14 October 2023

Keywords:
Hydrogen embrittlement
Hydrogen trapping
Transition metal carbides
Density functional theory
Migration barriers

ABSTRACT

Rapid developments in the field of hydrogen energy have prompted the need for safe and efficient hydrogen transportation and storage. Steels form the backbone of the current energy infrastructure and thus offer a fast and cost-effective solution. Their excellent mechanical properties are attributed to the underlying microstructure which comprises of finely dispersed nano-precipitates. However, one major factor restricting their application is their susceptibility to Hydrogen Embrittlement (HE). In the past decade, experimental and theoretical works have been carried out to understand if the nano-sized carbides can aid in reducing the susceptibility to HE along with providing strengthening. Within this ab-inito study, we investigated the effectiveness of fully coherent nano-carbides (i.e. TiC, VC and NbC) to limit the diffusible hydrogen content in bcc Fe. Our study revealed that the interplay between hydrogen and carbon vacancies, local atomic environment at interface as well as elastic strain fields at the interface can lead to significantly increased hydrogen solubilities. While in TiC, the deepest traps were found to be in the bulk of carbides, in VC and NbC, the elastic strain fields around the interface led to the strongest trapping. Further, the formation of a two-hydrogen-vacancy complex was found to be favourable in VC. Finally, the migration barriers for hydrogen trapping in bulk TiC as well as across the Fe/TiC coherent interface indicate that these deep traps in the form of carbon vacancies are fairly accessible.

© 2023 The Author(s). Published by Elsevier Ltd on behalf of Hydrogen Energy Publications LLC. This is an open access article under the CC BY license (http://creativecommons.org/licenses/by/4.0/).

* *Corresponding author.*
E-mail addresses: p.dey@tudelft.nl, poulumid@gmail.com (P. Dey).

https://doi.org/10.1016/j.ijhydene.2023.09.222

0360-3199/© 2023 The Author(s). Published by Elsevier Ltd on behalf of Hydrogen Energy Publications LLC. This is an open access article under the CC BY license (http://creativecommons.org/licenses/by/4.0/).

1. Introduction

The hydrogen economy is primed to play a significant role in the transition towards clean energy. From a materials perspective, solutions for safe and efficient hydrogen storage and transportation are highly sought after. Owing to their excellent mechanical properties, steels have formed the backbone of the current energy infrastructure. However, the interaction between hydrogen and steel can be quite unpredictable, and at worse, catastrophic. Since Johnson's experiments in 1875 [1], it is well known that even ppm levels of absorbed hydrogen can drastically reduce the strength and ductility of iron and steels. This degradation in mechanical properties of a material due to hydrogen is termed as hydrogen embrittlement (HE). The conditions that may lead to HE are ambiguous, as the degradation process occurs via a complex interplay between microstructure, stress state and environment. Consequently, several phenomenological models for HE have been developed [2–17]. A commonality in all of these models is the realization of a local critical hydrogen concentration at a critical zone in the microstructure (e.g. crack tip or void), beyond which the material fails rapidly.

Hydrogen that is dissolved in the steel matrix can be trapped at various lattice defects, such as vacancies, dislocations and grain boundaries [13,16]. Depending upon the magnitude of the trapping energy, the trapped hydrogen may or may not re-enter the steel matrix. Herein, a distinction is made between reversible and irreversible hydrogen traps. Hydrogen can be released from reversible traps at ambient temperatures while it remains trapped in irreversible traps. Thus, reversible traps can be seen to function as internal sources of hydrogen, while irreversible traps as sinks. A promising solution to improving the HE resistance of steels is to increase the concentration of irreversible traps [18–21] in the steel matrix. Although a precise distinction between reversible and irreversible traps is not evident, a binding energy of 0.6 eV or higher for the latter, as assigned by Pressouyre [22] is often considered as a defining critera. Some of the strongest hydrogen traps in steels are present in and around precipitates, and several experimental studies have shown that a homogeneous distribution of nano-sized transition-metal carbides can provide improved HE resistance [20,23–26]. These precipitates are a key constituent of Advanced High-Strength Steels (AHSS), as they provide significant strengthening via precipitation hardening.

The efficiency of precipitates as irreversible hydrogen traps depends on several factors, including stoichiometry [27], crystal structure [28] and coherency [29], as well as the local chemical environment of hydrogen [30]. The hydrogen trapping energy of precipitates can be estimated experimentally using Thermal Desorption Spectroscopy (TDS) [31–33] or Hydrogen Permeation Tests [21,34]. Depover et al. compared the trap strength of different carbides [32] and found that while TiC and V_4C_3 trapped hydrogen significantly, $Cr_{23}C_6$ and Mo_2C could only trap a comparatively small amount, while no hydrogen was trapped in W_2C. In TiC, hydrogen binding energies were found to reach up to 1.1 eV [31]. Apart from chemical composition, the size of the precipitate is also seen to affect trap strength. For small TiC that are coherent with the steel matrix ($<$ 5 nm), the deepest traps can be attributed to carbon vacancies in the bulk and at the carbide/matrix interface [20,35]. For larger, semi-coherent TiC, the misfit dislocation core at the interface is a deep trap while weaker traps are also present in the surrounding strain fields [33,36]. The deepest traps in incoherent TiC are present in the bulk, although a large activation energy is needed in order to populate these traps [31,37,38].

Advancements in the field of Atom Probe Tomography (APT) have made it possible to directly image hydrogen segregation around precipitates [39,40]. Takahashi et al. detected hydrogen isotopes at the semi-coherent interface of TiC and VC, while no segregation was seen around smaller coherent precipitates [39,41]. The trapping location was thus assumed to be either the misfit dislocation core or interface carbon vacancies. In subsequent work, the authors found that it was in fact the carbon vacancies at the interface between VC and the ferritic matrix that are the trapping sites [42]. In another APT study, deuterium was detected in the bulk of coherent VC [40]. In the case of incoherent NbC, deuterium segregated at the interface rather than in the bulk [43]. Both TDS and APT are subjected to several uncertainties and the preferential trapping of hydrogen in the bulk or at the interface of carbides is not evident. To this end, first-principles calculations have proven to be a useful tool to obtain accurate trapping energies and illuminate the underlying mechanism associated with trapping.

The trap strengths of various carbides and nitrides have been computed using Density Functional Theory (DFT). For each precipitate, there exists a wide range of trap energies that can be associated with the local atomic environment. In stoichiometric carbides of Group IV and V transition metals, it is found that the trigonal interstices are the strongest traps, however, they are significantly weaker than the interstices in bcc Fe [27,44–48]. Hydrogen segregation in such carbides is thus not likely. On the other hand, if the carbide contains a carbon vacancy, then the trapping is significantly stronger [27,47,49,50]. Additionally, the trap strength of a carbon vacancy decreases on moving from group IV to VI metals [50]. This is due to the coordination of the carbon vacancy, which facilitates a strong polar interaction between the trapped hydrogen and its nearest metal atoms [47].

With respect to the coherent interface between the carbides and bcc Fe, it is seen that the coherency strains at the interface can lower the trap energy of interstitial sites near the interface [27,48]. Yet, the interfaces only have weak trap sites and carbon vacancies must be present at the interface for irreversible trapping. However, the trap strength of carbon vacancies at the interface are different from those in bulk carbides. Moreover, significantly different values have been reported for hydrogen trapping around the interface, especially for the case of carbon vacancies [27,51]. Thus it is necessary to obtain a clear picture of the preferential segregation of hydrogen at the interface as compared with the bulk.

The activation energy for trapping and de-trapping of hydrogen can also be obtained with DFT, however they are not as commonly studied. Di Stefano et al. reported a barrier of 1.7 eV for hydrogen to migrate from a vacancy to a nearby interstice in bulk TiC [27]. The high value of de-trapping

barrier confirms the irreversibility of trapping in bulk carbon vacancies. Given the considerable difference between trapping energy at an interface vacancy and one in the bulk of the carbide, the barriers to the migration of hydrogen across the coherent interface can be expected to be quite different.

In this work, we perform a DFT study on hydrogen segregation and migration in bulk TiC, VC and NbC as well as their coherent interfaces with α-Fe. Firstly, with the help of various charge analysis methods, we make a thorough comparison between the trapping and bonding interactions in the three carbides, which helps us to describe the trap strength of various local atomic environments more generally. We also consider the likelihood of formation of hydrogen-vacancy complexes, such as those which are common in FCC metals [52]. In the next step, the trapping of hydrogen at interface vacancies is compared with that in the bulk. Finally, the activation energies for hydrogen trapping and de-trapping into and from the deepest traps are calculated. The paper is organised as follows: in section 2, the theoretical framework and technical details of the DFT calculations are presented. In section 3, the results for hydrogen trapping in bulk phases, hydrogen-vacancy complex formation, trapping at coherent interfaces and the corresponding hydrogen migration barriers are discussed. Finally, the most important conclusions are drawn in section 4.

2. Methodology

2.1. Theoretical framework

TiC, VC and NbC have the rock salt (B1) crystal structure. Small precipitates are known to be fully coherent with the bcc Fe matrix and follow the Baker-Nutting orientation with (001)Fe ‖ (001)MC and [100]Fe ‖ [110]MC, where M = Ti, V and Nb. DFT was employed to identify the respective ground state structures of the metal carbides (MC) and the Fe/MC coherent interfaces. Before calculating the hydrogen trapping energy in the carbides, the solution enthalpy of hydrogen in bcc Fe was calculated according to equation:

$$E_H^{Fe} = E[FeH] - E[Fe] - \frac{1}{2}\mu_{H_2}^0, \quad (1)$$

where, $E[FeH]$ and $E[Fe]$ are the DFT-obtained energies of a bcc Fe supercell with and without a hydrogen atom respectively, and $\mu_{H_2}^0$ is the chemical potential of a hydrogen molecule. The chemical potential of hydrogen was calculated as the energy of an isolated hydrogen molecule in a cube of size 8 Å. We found the tetrahedral interstices to be preferable over the octahedral ones. Next, the segregation of hydrogen in bulk carbides and at the coherent interface was calculated according to equation:

$$E_{seg}^i = E[MCH_i] - E[MC] - [E[FeH] - E[Fe]], \quad (2)$$

where $E[MCH_i]$ is the DFT-obtained energy of a metal carbide system with a hydrogen atom segregated at trap i, $E[MC]$ is the energy of the system without hydrogen segregation and $E[FeH]$ is the total energy of the bcc Fe supercell with hydrogen in the tetrahedral interstice. By this definition, we consider the source of hydrogen to be the Fe matrix. Thus E_{seg}^i determines the tendency of hydrogen to segregate from the Fe matrix into trap i. Negative values of E_{seg}^i indicate preferential segregation of hydrogen in the trap i, and therefore stronger trapping.

Since these carbides are known to be off-stoichiometric [53–57], carbon and metal vacancies were considered in this work alongside several interstitial trap sites. To estimate the likelihood of having a carbon vacancy in the carbide, the carbon vacancy formation energy within bulk carbides and at the coherent interface was calculated according to equation:

$$E_{vac}^C = E[M_nC_{n-1}] - E[M_nC_n] + \mu_C^0, \quad (3)$$

where $E[M_nC_{n-1}]$ is the energy of the system with one carbon vacancy (and n atoms of M), $E[M_nC_n]$ is the energy of the stoichiometric system and μ_C^0 is the chemical potential of carbon, taken here as the energy of a carbon atom in its ground state of graphite. Thus, a lower value of E_{vac}^C implies stronger tendency to form a carbon vacancy. Next, the formation energy of a multiple hydrogen - vacancy complex was calculated as per equation:

$$E_f^{Hvac} = E_{vac}^{nH} - E[MC] + \mu_C^0 - n[E[FeH] - E[Fe]], \quad (4)$$

where E_{vac}^{nH} is the energy of a supercell with a vacancy and n hydrogen atoms surrounding the vacancy and $E[MC]$ is the energy of the vacancy-free supercell without any hydrogen atoms. The hydrogen - vacancy complex formation energy described thus, involves the formation of a carbon vacancy in an ideally stoichiometric carbide and subsequent dissolution of n hydrogen atoms in the vacancy. Another common way to describe multiple hydrogen - vacancy complexes is via the incremental hydrogen segregation energy in a vacancy, given by equation:

$$E_{seg}^n = E_{vac}^{nH} - E_{vac}^{(n-1)H} - [E[FeH] - E[Fe]] \quad (5)$$

Further, several DFT-based charge analysis methods such as Density of States (DOS), Electron Localization Function (ELF) [58] and Bader charge partitioning [59–61], along with the Crystal Orbital Hamiltonian Population (COHP) [62–64] analysis were utilised.

2.2. Computational details

All DFT calculations were performed using the Vienna Ab-initio simulation package (VASP) [65]. Generalized gradient approximation (GGA) in the formulation of Perdew, Burke, and Ernzerhof (PBE) was used for the exchange-correlation function [66], while the Projector Augmented Wave (PAW) method was used for the core-valence interactions [67]. A cut-off energy of 500 eV was implemented in all calculations. For the bulk Fe calculations, a 16-atom 2 × 2 × 2 supercell was used. A 64-atom 2 × 2 × 2 supercell was used for bulk carbide calculations while an 80-atom supercell was used for the coherent interface (see Figs. 1 and 5). The Brillouin zone was sampled using Monkhorst-Pack grids [68]. For bcc Fe, a 12 × 12 × 12 k-mesh was employed. A 6 × 6 × 6 k-mesh was used for all MC systems (bulk) while the Fe/MC (interface) systems were sampled with a 8 × 8 × 2 k-mesh. The chosen supercell size, cut-off energy and k-mesh density were tested to be well

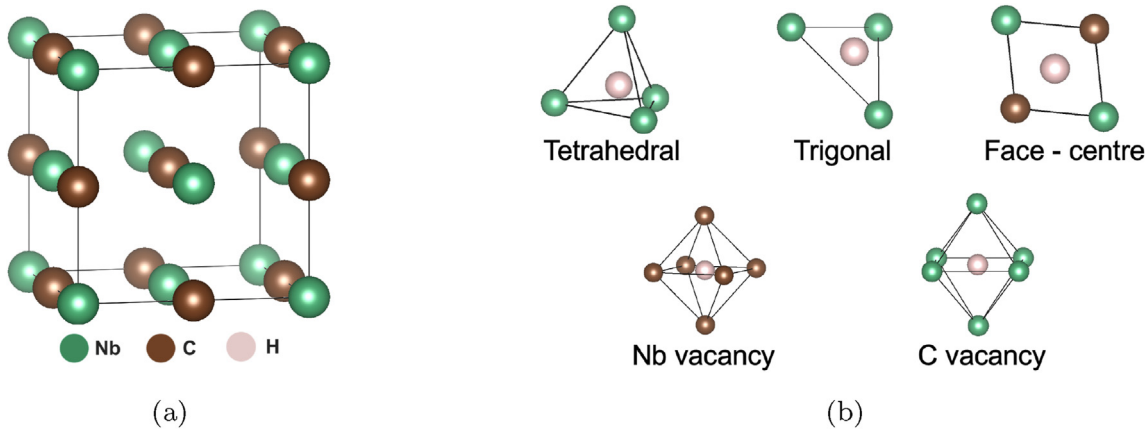

Fig. 1 – (a) A unitcell of NbC depicting the rocksalt structure. Niobium atoms are in an fcc lattice while the carbon atoms occupy all octahedral voids, and, (b) the geometry of various trap sites considered in this work. TiC and VC have the same structure.

converged within 0.01 eV/atom. The first-order Methfessel-Paxton method was used for the Fermi-surface smearing [69]. A smearing width of 0.15 eV was chosen such that the corresponding error in the 0-K extrapolated energy is less than 1 meV/atom. The energy tolerance for the electronic self-consistency loop was set as 10^{-6} eV. Since bcc Fe is ferromagnetic, all bulk Fe and interface calculations were carried out as spin-polarized while the calculations on bulk carbides were non-spin-polarized. All lattice vectors and atom positions were relaxed until the residual forces on each atom were below 0.01 eV/Å. Migration barriers were calculated using the climbing image - Nudged Elastic band (CI-NEB) method [70,71]. With this method, an interpolated chain of images between the initial and final states is connected by a spring and relaxed simultaneously to obtain the minimum energy path and activation barrier. Five images were used for bulk carbides whereas three images were used for the interface calculations. Same convergence criteria as the aforementioned DFT calculations were used.

3. Results

3.1. *Segregation in bulk carbides*

The obtained lattice parameters of TiC, VC and NbC were 4.33 Å, 4.16 Å and 4.48 Å respectively, which agree very well with experimental values [72]. Firstly, the solubility of hydrogen in these carbides is discussed. The various trap sites are depicted in Fig. 1. The tetrahedral and face-centre positions are cubic interstitial voids, while the trigonal site is the void formed in between three metal atoms in the (111) plane. The other two positions are substitutional, namely a metal and a carbon vacancy. The segregation energy of hydrogen in all these positions is listed in Table 1.

It can be seen that none of the interstitial voids are favourable sites for hydrogen trapping, although the trigonal sites are most preferable. This stronger binding in trigonal sites has previously been attributed to a covalent bond formation between hydrogen and the nearest carbon atom [45, 47]. We found that the C–H distances in the fully relaxed state are 1.16 Å, 1.15 Å and 1.14 Å for TiC, VC and NbC respectively. For such short distances, a C–H bond formation is highly likely. In Fig. 2, two-dimensional section images of the Electron Localization Function (ELF) obtained for a hydrogen atom dissolved at the various interstitial positions and a carbon vacancy in VC are shown (similar results were observed for TiC and NbC, which are not discussed here separately for brevity). ELF describes the probability of finding an electron pair in a given region in space. Since electron pairs can be found in covalent bonds and lone pairs or filled valence shells, ELF is a useful tool in imaging covalent bonding interactions. When hydrogen is in one of the interstices, there is some degree of electron pair localization in the space between the hydrogen atom and the nearest carbon atom(s). This is indicative of a covalent interaction between the two species, resulting from the overlap of bonding orbitals [58]. This feature is most prominent at the trigonal site (Fig. 2b), where overlap of the atomic orbitals of carbon and hydrogen can be

Table 1 – Segregation energy of hydrogen in the three carbides. The literature values are form previously reported DFT calculations.

Type	Position	Segregation energy (eV)	Literature
TiC	Tetrahedral	1.19	1.45 [45], 0.97 [49]
	Trigonal	0.73	0.84 [27], 0.99 [45]
	Face-centre	1.39	–
	C vacancy	−1.09	−1.16 [49], −1.17 [50]
	Ti vacancy	1.51	–
VC	Tetrahedral	1.91	2.08 [45], 2.11 [46]
	Trigonal	1.38	1.57 [45], 1.55 [48]
	Face-centre	1.73	–
	C vacancy	−0.16	−0.37 [50], −0.03 [48]
	V vacancy	2.06	–
NbC	Tetrahedral	2.07	2.14 [45], 1.65 [48]
	Trigonal	1.45	1.59 [45]
	Face-centre	2.07	–
	C vacancy	−0.20	−0.28 [50], −0.00 [48]
	Nb vacancy	2.26	–

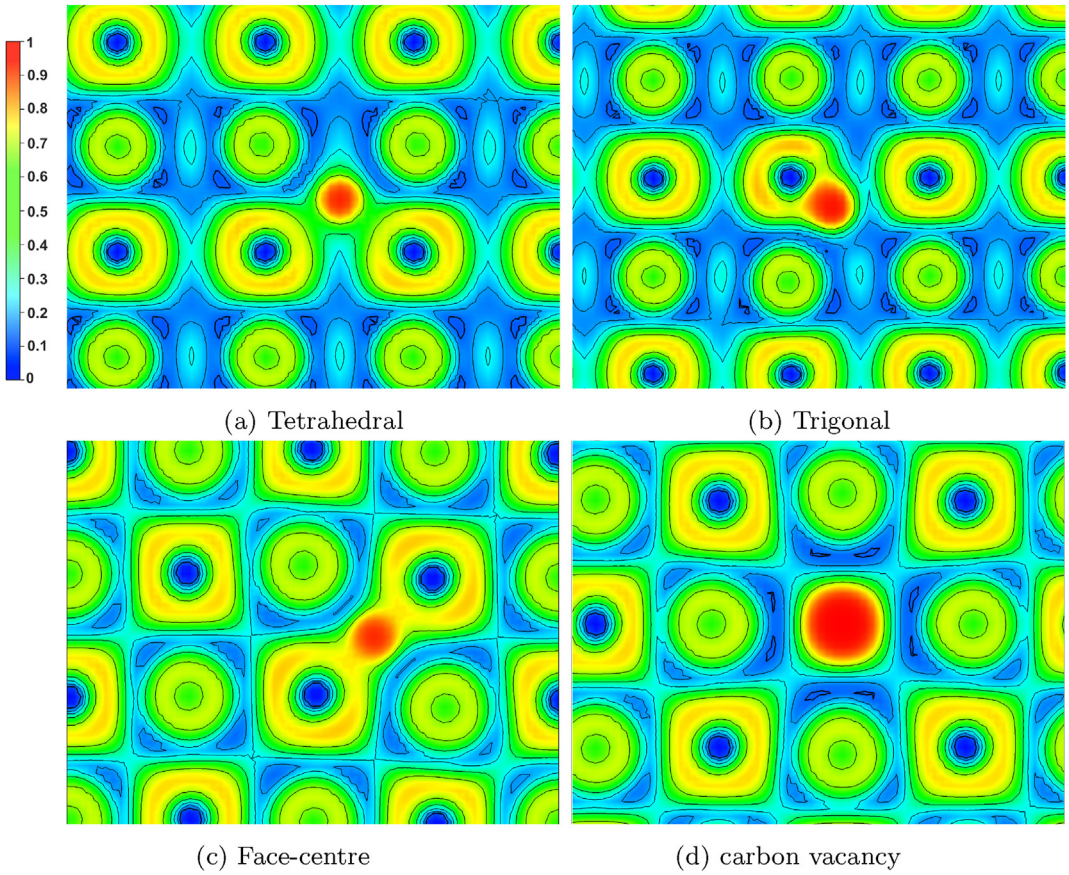

Fig. 2 – 2D slices of the Electron Localization Function (ELF) in VC, with hydrogen in various positions in the bulk carbide. The spherical contours belong to the metal atoms, the elongated contours are carbon atoms and the hydrogen atom is seen as the red spherical region. (For interpretation of the references to color in this figure legend, the reader is referred to the Web version of this article.)

seen. This explains the preference for trigonal voids as compared to the other interstitial sites. From the corresponding partial density of states analysis, the bonding orbitals were identified as C-2s and H-1s (see appendix Figure A2).

Contrary to the interstitial sites, the ELF image for hydrogen at a carbon vacancy is markedly different (Fig. 2d). In this case, the regions between the C and H atoms do not show any electron pair localization. However, the high ELF region around the H atom is significantly larger than that in the other positions. Simultaneously, low ELF regions are seen around the nearest metal atoms. This is possible if there is a partial charge transfer from the six nearest metal atoms (four in plane and two out of plane) towards the H atom which causes the stretching out of the high ELF region around H in all six directions. Referring to Table 1, the segregation energy of hydrogen in a carbon vacancy is exothermic. We had previously seen the absence of any covalent interactions involving hydrogen at carbon vacancy positions. Moreover, the volumetric strain upon the formation of, and subsequent dissolution of hydrogen in the carbon vacancy is negligible (we obtain a volumetric expansion of 0.07% for TiC). The strong binding thus points towards a more polar interaction between hydrogen and the neighbouring atoms. The change in charge density upon the addition of hydrogen in a carbon vacancy was obtained by subtracting from the total charge density, the charge density of its constituents (see equation (6) below).

$$\Delta\rho = \rho_{MCH} - \rho_{MC} - \rho_{H} \tag{6}$$

The charge density difference results thus obtained are shown in Fig. 3. Charge transfer between the species is apparent, with charge depletion around the six nearest metal atoms (two out of plane), and accumulation around the hydrogen atom. Thus, by strong polar interactions with its nearest metal atoms, the hydrogen atom can be trapped rather strongly at a carbon vacancy. Moreover, the extent of charge transfer is highest in TiC and lowest in NbC. However, as can be seen in Table 1, while the hydrogen segregation energy is lowest in TiC, that in NbC is lower than in VC. Thus the ionic charge in itself is not sufficient to determine the trap strength. It has been reported that the Bader atomic volume of hydrogen has a stronger correlation with the segregation energy [47,51]. We also found the assertion to be valid for bulk carbides (see appendix Figure B1).

The apparent trapping capacity of carbides may be higher, if multiple hydrogen atoms can be trapped in a single vacancy.

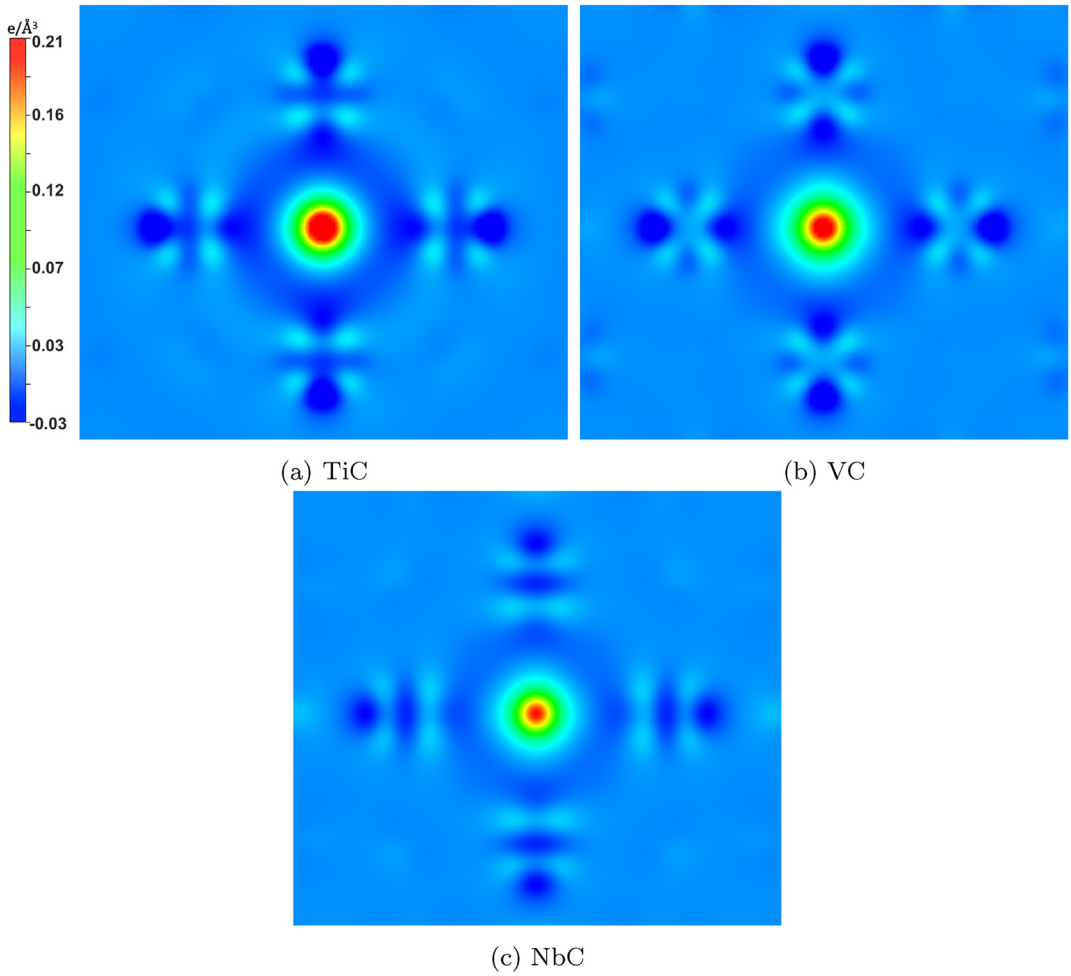

Fig. 3 – 2-D sections of the charge density difference when hydrogen is dissolved in a carbon vacancy. Units are in electrons/Å³.

Multiple hydrogen - vacancy complexes are discussed in the following section.

3.2. *Multiple hydrogen - vacancy complex formation*

Likely formation of hydrogen-vacancy complexes have been reported for several fcc metals [52,73] as well as in TiC [49]. In the rocksalt structure, each carbon vacancy is surrounded by eight closest tetrahedral voids, which can be occupied by hydrogen atoms. When a single hydrogen atom is placed in any of these positions, it moves into the centre of the vacancy upon structural relaxation. However, when multiple sites are occupied simultaneously, stable hydrogen-vacancy complexes may form. Ding et al. reported that up to four hydrogen atoms can cluster around a single carbon vacancy [49]. The multiple hydrogen-vacancy complex formation energy and incremental hydrogen segregation energy as calculated by equations (4) and (5) respectively are listed in Table 2. Up to four hydrogen-vacancy complexes were studied and only the most stable configuration for each complex from Ref. [49] are considered.

There is a marked difference in our results for segregation energy in TiC as compared to Ding. et al. [49]. There are two possible reasons for this: firstly, we use a larger supercell so as to avoid defect-image interaction arising from periodic boundary conditions, and secondly, we use a larger value of the cut-off energy. The formation energy of a 1H-Vac complex was found to be exothermic for all three carbides. Moreover, for VC, the formation of 2H-Vac complex is also exothermic. Even though TiC has the strongest hydrogen trapping in the

Table 2 – Multiple H-Vac complex formation energy and incremental segregation energy of hydrogen atoms in a vacancy. The values in brackets are those reported by Ding et al. [49].

Complex	E_f^{Hvac} (eV)			E_{seg}^{n} (eV)		
	TiC	VC	NbC	TiC	VC	NbC
1H-Vac	−0.37	−0.92	−0.25	−1.09 (-1.16)	−0.17	−0.20
2H-Vac	0.45	−0.02	0.28	−0.28 (-0.71)	0.73	0.33
3H-Vac	1.41	1.25	1.09	0.68 (-0.05)	2.01	1.15
4H-Vac	2.03	2.26	1.66	1.30 (0.04)	3.02	1.72

carbon vacancy, the vacancy formation energy is much higher than in VC and NbC, which cancels out in the complex formation energy. It is often useful to plot the H-Vac complex formation energy as a function of the chemical potential of hydrogen. Such a plot for VC is shown in Fig. 4. The 0-H line simply corresponds to the vacancy formation energy. Firstly, it can be seen that the vacancy formation energy in VC is negative. This implies that the VC structure is unstable against a carbon vacancy formation. In stoichiometric VC, the antibonding orbitals are also occupied and thus the removal of carbon atoms makes the structure more stable. It is found that VC exists as V_4C_3 and V_6C_5 [74,75]. For low chemical potentials up to −0.15 eV, hydrogen dissolution in the carbon vacancy is not favourable. From −0.15 to +0.95 eV, the 1H-Vac complex is the most stable phase. At higher chemical potentials, the 2H-Vac complex is favourable while the 4H-Vac complex will form above 1.2 eV. Thus multiple H-vac complexes can form only under conditions of high chemical potential.

As a next step, hydrogen trapping around the carbide-matrix interface is discussed. The interface can be fully coherent, semi-coherent or incoherent, depending upon the size of the carbide particle [76]. In this work, we focus only on the coherent interface, as nano-carbides that are seen to help with hydrogen embrittlement are within the size range of the coherent interface [24–26].

3.3. *Coherent interface*

The coherent interface between bcc Fe and rocksalt TiC, VC and NbC is in the Baker-Nutting Orientation [77]. The orientation and simulation cell are depicted in Fig. 5. The supercell dimensions were chosen based on existing work, wherein the size of the supercell was optimised with respect to the solution enthalpy of hydrogen [27,51]. Once again, several trap sites at the interface as well as adjacent atomic layers were studied. Here, the interface is considered as the region in between (and including) the closest Fe and carbide layers.

Due to the lattice mismatch between Fe and carbide, the Fe matrix tends to adapt to the lattice parameters of the spnger carbide. Upon full relaxation of the interface, we obtained a volumetric lattice strain of 2%, 2.2% and 3.6% in TiC, VC and NbC respectively. Moreover, upon structural relaxation, the planar alignment of metal and carbon atoms in the carbide layer was slightly distorted. This phenomenon has been previously reported in both theoretical and experimental studies and is known as rippling [78,79]. In the Fe matrix, the Fe–Fe distance in the direction perpendicular to the interface plane was found to change gradually. For the Fe atoms that were directly below the carbon atoms, the Fe–Fe distance increased upon moving farther away from the interface and reciprocally, decreased for the Fe atoms directly below the Nb atoms. These structural changes in the Fe and carbide layers were seen to affect the segregation of hydrogen. The segregation of hydrogen at various positions around the interface is listed in Table 3. Tetrahedral, octahedral and carbon vacancy sites were considered within the region comprising the interface in Fig. 5. Several *bulk-like* positions in the Fe and carbide matrix in the adjacent atomic layers were also taken into account. These include the tetrahedral and octahedral interstices in the Fe matrix and the tetrahedral and trigonal interstices along with a carbon vacancy in the bulk carbide.

Firstly, consider the tetrahedral interstices in the Fe layers. It is seen that for all carbides, the segregation of hydrogen in the first and third Fe layers is enhanced, while that in the second Fe layer is slightly reduced. A segregation energy of −0.42 eV was obtained for the first Fe layer in NbC, which is even slightly higher than that in a carbon vacancy in bulk NbC. Due to the disparity in the Fe–Fe distances arising from lattice rippling, the three tetrahedral positions are not equivalent, and have different void volumes. Consequently, different segregation energies are obtained. Moreover, the relative segregation energy is highest for NbC, which also has the largest lattice mismatch. Thus, the enhanced segregation in the tetrahedral sites can be attributed mainly to the coherency strains. The octahedral voids, which have a smaller volume than the tetrahedral voids, still remain unfavourable.

Secondly, consider the segregation of hydrogen at the interface. For all the carbides, the segregation energy in tetrahedral voids is lowered, with the decrease being substantial in NbC. The segregation energy of −0.31 eV is again, lower than that in bulk carbon vacancies in NbC. Thus, for NbC, deeper traps exist in the form of tetrahedral voids

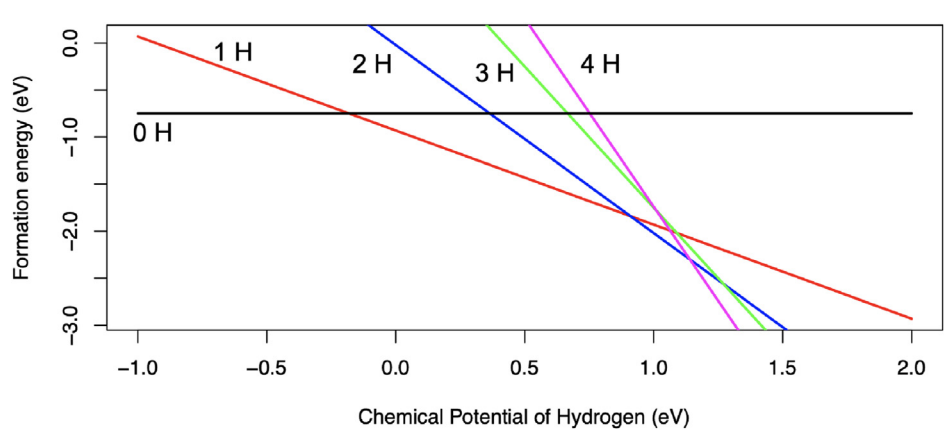

Fig. 4 – The formation energy of 0, 1, 2, 3 and 4 hydrogen-vacancy complexes as a function of the chemical potential of hydrogen in VC, as calculated using equation (4). The chemical potential of hydrogen in a tetrahedral void in bcc Fe is set to zero and is marked with the dashed vertical line.

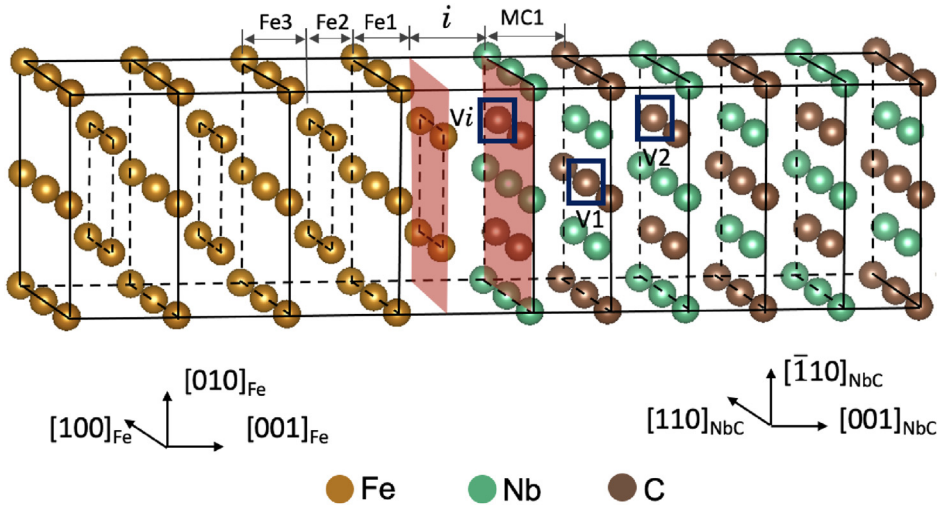

Fig. 5 – The carbide-Fe coherent interface with the Baker-Nutting orientation relation. The region enclosed between the planes is the interface region and referred as i. Hydrogen segregation energy was calculated at various atomic layers in the Fe and carbide sub-matrix. $V_{i/1/2}$ are carbon vacancy positions in the carbide layers.

around the coherent interface, rather than in the bulk. The segregation of hydrogen in octahedral voids is also enhanced, but only very slightly. In both these positions, the hydrogen atom is directly coordinated with species from both the bulk phases. In such cases, along with the elastic strains at the interface, the unique chemical environment also contributes to the segregation energy. However, a comparison with the interstitial sites in the Fe layers indicates that the elastic effect is still dominant.

Thirdly, the segregation energy at the interface carbon vacancy is the lowest in TiC and that in VC and NbC is comparable. However, differing trends are seen in the hydrogen solubility at a interface vacancy as compared to the bulk. For VC and NbC, the segregation energy is substantially lower at the interface than that in bulk carbides, whereas the change is relatively minor for TiC. At the interface vacancy, the hydrogen atom is coordinated by five Ti, V or Nb atoms and one Fe atom as opposed to six Ti, V or Nb atoms in bulk vacancies. Since the trapping of hydrogen in vacancies is mediated by polar interactions, it may be expected that at the interface, the chemical effect due to an Fe atom has a major contribution to the segregation energy. In order to quantify the chemical effect at the interface, we performed Crystal Orbital Hamiltonian Population (COHP) analysis on the three carbides. COHP reflects the strength of bonding between a pair of atoms. The Integrated-COHP value of the Fe–H interaction was found to be −0.77 in VC, as compared to −0.52 in TiC (see appendix section C). Thus, the chemical effect of the Fe–H

Table 3 – Segregation energy (in eV) of hydrogen in various positions around the coherent interface. The positions are labelled as Type(Octahedral, Tet, or C Vacancy) and phase (Fe or MC) followed by the number of atomic layer away from the interface (1, 2, 3 or interface).

Position	Carbides		
	TiC	VC	NbC
Tet Fe 3	−0.07	−0.20	−0.24
Oct Fe 2	0.22	0.10	0.36
Tet Fe 2	0.05	−0.03	0.10
Oct Fe 1	0.45	0.30	0.53
Tet Fe 1	−0.11	−0.13	−0.42
	(-0.30 [51], −0.32 [27])	(-0.11 [51])	(-0.30 [51], −0.28 [48])
Oct i	0.00	−0.08	0.27
	(-0.15 [51], −0.10 [48])	(-0.10 [48],-0.12 [51])	
Tet i	−0.12	−0.11	−0.31
	(-0.28 [51], −0.32 [27])	(-0.14 [51], −0.11 [48])	(-0.20 [51], −0.15 [48])
Vac i	−1.07	−0.53	−0.50
	(-0.46 [27], −1.02 [51])	(-0.38 [80], −0.58 [48,51])	(-0.55 [48,51])
Vac 1	−0.99 (−0.86 [27])	−0.55 (−0.41 [80])	−0.49
Vac 2	−1.05 (−0.88 [27])	−0.45	−0.39
Tet MC 1	0.84	1.99	2.03
Tri MC 1	1.15	0.99	1.66

Table 4 – Carbon vacancy formation energy (in eV) at the interface (i) and adjacent carbide layers. Refer to Fig. 5 for exact positions. Bulk refers to the vacancy formation energy in bulk carbide supercells.

Carbide	Position			
	Vac i	Vac 1	Vac 2	Bulk
TiC	1.04	0.89	0.85	0.74
VC	0.26	0.08	−0.32	−0.79
NbC	0.67	0.45	0.17	−0.05

Table 5 – Hydrogen migration barriers in TiC (in eV).

Bulk Trapping	Bulk De-trapping	Interface Trapping	Interface De-trapping
0.16	2.75	0.13	0.92

interaction is stronger in VC than in TiC. The reduction in segregation energy of hydrogen at the interface vacancy is therefore lower in VC than in TiC. However, when considering carbon vacancies at and around the interface, it is also critical to know whether or not such a vacancy is likely to form at all.

The vacancy formation energy at different carbide layers near the interface was calculated according to equation (3) and are listed in Table 4. The vacancy formation energy was found to be significantly higher at the interface than in the bulk. The Fe–C interaction across the interface is known to be strongly covalent [81], which makes it more difficult to create vacancies at the interface. Thus, although VC and NbC may have deep traps at the interface in the form of carbon vacancies, their concentration is significantly smaller than that in the bulk.

Finally, the segregation of hydrogen in the tetrahedral and trigonal interstices in the carbide layer still remains unfavourable. Thus, in conclusion, we find that along with the carbon vacancies, the tetrahedral voids at the interface and the nearest Fe layer can also be deep traps for hydrogen, owing to the elastic strains from the lattice mismatch between the two bulk phases.

3.4. *Migration barriers in TiC*

In order to reduce the effective diffusivity of hydrogen, carbon vacancies in the bulk or at the interface must be able to trap the hydrogen atoms. Migration barriers between equivalent trap sites have been calculated for bulk VC [44]. The lowest barriers for hydrogen migration between nearest trigonal sites was 0.19 eV, while that between adjacent carbon vacancies was found to be 2.12 eV. In TiC, Ding et al. reported a value of 1.19 eV for migration between adjacent vacancies [49]. In this work, we calculated the migration barriers between a carbon vacancy and an interstitial void in TiC. Two different scenarios were considered: firstly, when a hydrogen atom is diffusing through the interstitial sites in bulk TiC and encounters a carbon vacancy, and secondly, when the hydrogen atom is in the Fe matrix of a Fe/TiC coherent interface, and encounters a carbon vacancy at the interface. For the first case, we considered the migration of hydrogen into a vacancy from a second-nearest tetrahedral site (The barrier from nearest tetrahedral sites is zero). The smallest migration barriers are listed in Table 5. In bulk TiC, the migration barrier for trapping was found to be 0.16 eV while for de-trapping it

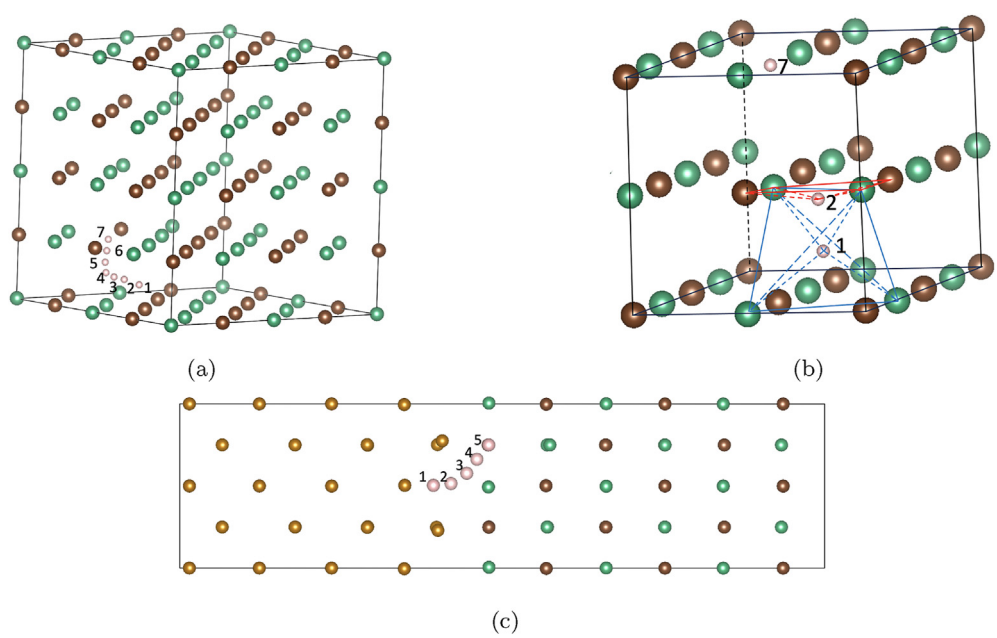

Fig. 6 – Minimum energy path for trapping and detrapping in a vacancy from nearby tetrahedral site in (a) bulk TiC and (c) Fe/TiC interface. The tetrahedral site is labelled as 1 and the vacancy as 7 in bulk TiC and 5 in Fe/TiC interface. b) Zoomed in view of the initial (1) and final (7) position and the saddle point (2) in bulk TiC. The initial tetrahedral site is marked in blue. The saddle point resembles a face-centre configuration (shown in red). (For interpretation of the references to color in this figure legend, the reader is referred to the Web version of this article.)

was 2.75 eV. The barrier for de-trapping was significantly high, which indicates the irreversible nature of trapping. The minimum energy path is shown in Fig. 6 a and b. The transition state was identified as a face-centre void, which was also reported in Ref. [44] for hydrogen migration between adjacent vacancies in VC. For the second case, we considered the migration of hydrogen into a carbon vacancy at the interface from the tetrahedral void in the first Fe layer adjacent to the interface. The minimum energy path is shown in Fig. 6c. The migration barrier for trapping in a carbon vacancy was found to be 0.13 eV and is comparable to that in bulk TiC. The barrier for de-trapping was found to be 0.92 eV, which although still a high value, is smaller than that in bulk TiC. Thus, the most irreversible traps can be said to lie in the bulk of the carbides.

4. Conclusion

Using a variety of charge analysis methods in combination with DFT, we were able to study the segregation and migration of hydrogen in transition metal carbides. We observed that in stoichiometric carbides, hydrogen binds covalently with the carbon atoms, provided the C–H distance is relatively small. ELF images indicated clear overlap between the spherical s orbital of carbon the s orbital of hydrogen. Yet these are not favourable traps and carbon vacancies are the only deep traps in bulk carbides. When hydrogen occupies a carbon vacancy, a polar bond is formed between the hydrogen atom and its six neighbouring metal atoms, which leads to strong trapping. The strength of trapping is determined by the charge transfer between the species as well as the associated volume over which the charge is localised. The segregation energy of hydrogen in a carbon vacancy in TiC is substantially low (−1.09 eV). In all the three carbides, it is easier to form a hydrogen-vacancy complex than a vacancy without hydrogen. However, VC has lowest hydrogen-vacancy complex formation energy. This is due to the already low vacancy formation energy in VC, which are known to precipitate as V_4C_3 and V_6C_5. Moreover, a single vacancy in VC can also trap up to two hydrogen atoms favourably. The formation of other multiple hydrogen-vacancy complexes requires a relatively high chemical potential of hydrogen and is typically not feasible.

We also studied segregation of hydrogen around the coherent carbide/bcc-Fe interface. The lattice mismatch between the two phases caused coherency strains near the interface. This lead to some enhancement in segregation in the Fe matrix adjacent to the interface. NbC depicted the largest change, with a tetrahedral void in the immediate Fe layer having a segregation energy of −0.42 eV. This is even lower than the segregation energy in a carbon vacancy in bulk NbC. Thus, in NbC, deep traps are present in the elastic strain fields around the interface. Notably, the segregation energy at the interface vacancies was found to be substantially lower than that in the carbon vacancies in bulk VC and NbC. At this position, in addition to the polar V–H or Ti–H bonds, the hydrogen atom is also stabilised by the Fe–H bond at the interface. COHP analysis of the Fe–H bond at the interface revealed a stronger Fe–H bond in VC than in TiC, which led to the lower segregation energy at the interface vacancy in VC than one in the bulk.

In regard to the migration barriers for hydrogen in TiC, it was found that within the bulk TiC, a moderately low activation energy of 0.16 eV is needed for hydrogen to jump into a carbon vacancy from a trigonal site. Moreover, the de-trapping barrier was found to be 2.75 eV, which indicates towards the irreversible nature of hydrogen trapping in carbon vacancies. Across the interface, the migration barrier for hydrogen to jump from a tetrahedral interstices in bcc Fe into an interface vacancy was found to be comparable to that in the bulk. The de-trapping barrier was lower than that in the bulk, however the obtained value of 0.92 eV is still high so as to form an irreversible trap.

In conclusion, we have found that off-stoichiometric TiC precipitates are the most effective irreversible hydrogen traps by virtue of strong Ti–H polar interactions. On the other hand, the coherency strains from NbC, which has a larger lattice parameter than TiC and VC, can also enhance the segregation of hydrogen in the tetrahedral interstices around the interface. Thus while in TiC, the deepest traps lie in the bulk of the precipitate, in NbC and VC, tetrahedral voids at the interface are the deepest traps. Carbon vacancies at the interface are also found to be one of the deepest traps, although the formation of such vacancies is highly unlikely. The migration barriers for trapping in carbon vacancy were found to be quite low thereby indicating that these traps are relatively accessible. The high de-trapping barriers reflect the irreversible nature of trapping.

Acknowledgements

The authors would like to thank Tata Steel Europe for sponsoring this research. This project was carried out under project number N19009 in the framework of the Partnership Program of the Materials Innovation Institute M2i (www.m2i.nl) and the Netherlands Organization for Scientific Research (www.nwo.nl). This work was facilitated by NWO Domain Science for the use of supercomputer facilities. The authors also acknowledge the use of DelftBlue supercomputer [82], provided by Delft High Performance Computing Centre (https://www.tudelft.nl/dhpc).

Appendix A. Supplementary data

Supplementary data to this article can be found online at https://doi.org/10.1016/j.ijhydene.2023.09.222.

REFERENCES

[1] Johnson WH. On some remarkable changes produced in iron and steel by the action of hydrogen and acids. Proc Roy Soc Lond 1875;23(156–163):168–79. https://doi.org/10.1098/rspl.1874.0024.
[2] Nagumo M, Yagi T, Saitoh H. Deformation-induced defects controlling fracture toughness of steel revealed by tritium desorption behaviors. Acta Mater 2000;48(4):943–51. https://doi.org/10.1016/s1359-6454(99)00392-4.
[3] Nagumo M, Takai K. The predominant role of strain-induced vacancies in hydrogen embrittlement of steels: Overview.

Acta Mater 2019;165:722–33. https://doi.org/10.1016/j.actamat.2018.12.013.
[4] Nagao A, Smith CD, Dadfarnia M, Sofronis P, Robertson IM. The role of hydrogen in hydrogen embrittlement fracture of lath martensitic steel. Acta Mater 2012;60(13–14):5182–9. https://doi.org/10.1016/j.actamat.2012.06.040.
[5] Hirth JP. Effects of hydrogen on the properties of iron and steel. Metall Trans A 1980;11(6):861–90. https://doi.org/10.1007/bf02654700.
[6] Momotani Y, Shibata A, Terada D, Tsuji N. Effect of strain rate on hydrogen embrittlement in low-carbon martensitic steel. Int J Hydrogen Energy 2017;42(5):3371–9. https://doi.org/10.1016/j.ijhydene.2016.09.188.
[7] Matsumoto Y, Miyashita T, Takai K. Hydrogen behavior in high strength steels during various stress applications corresponding to different hydrogen embrittlement testing methods. Mater Sci Eng, A 2018;735:61–72. https://doi.org/10.1016/j.msea.2018.08.002.
[8] Birnbaum H, Sofronis P. Hydrogen-enhanced localized plasticity—a mechanism for hydrogen-related fracture. Mater Sci Eng, A 1994;176(1–2):191–202. https://doi.org/10.1016/0921-5093(94)90975-x.
[9] Sofronis P, Birnbaum H. Mechanics of the hydrogendashdislocationdashimpurity interactions—i. increasing shear modulus. J Mech Phys Solid 1995;43(1):49–90. https://doi.org/10.1016/0022-5096(94)00056-b.
[10] Robertson I. The effect of hydrogen on dislocation dynamics. Eng Fract Mech 2001;68(6):671–92. https://doi.org/10.1016/s0013-7944(01)00011-x.
[11] von Pezold J, Lymperakis L, Neugebeauer J. Hydrogen-enhanced local plasticity at dilute bulk h concentrations: the role of h–h interactions and the formation of local hydrides. Acta Mater 2011;59(8):2969–80. https://doi.org/10.1016/j.actamat.2011.01.037.
[12] Barnoush A, Vehoff H. Recent developments in the study of hydrogen embrittlement: hydrogen effect on dislocation nucleation. Acta Mater 2010;58(16):5274–85. https://doi.org/10.1016/j.actamat.2010.05.057.
[13] Kirchheim R. On the solute-defect interaction in the framework of a defactant concept. Int J Mater Res 2009;100(4):483–7. https://doi.org/10.3139/146.110065.
[14] Kirchheim R. Solid solution softening and hardening by mobile solute atoms with special focus on hydrogen. Scripta Mater 2012;67(9):767–70. https://doi.org/10.1016/j.scriptamat.2012.07.022.
[15] Deng Y, Barnoush A. Hydrogen embrittlement revealed via novel in situ fracture experiments using notched micro-cantilever specimens. Acta Mater 2018;142:236–47. https://doi.org/10.1016/j.actamat.2017.09.057.
[16] Barrera O, Bombac D, Chen Y, Daff TD, Galindo-Nava E, Gong P, Haley D, Horton R, Katzarov I, Kermode JR, Liverani C, Stopher M, Sweeney F. Understanding and mitigating hydrogen embrittlement of steels: a review of experimental, modelling and design progress from atomistic to continuum. J Mater Sci 2018;53(9):6251–90. https://doi.org/10.1007/s10853-017-1978-5.
[17] Neeraj T, Srinivasan R, Li J. Hydrogen embrittlement of ferritic steels: Observations on deformation microstructure, nanoscale dimples and failure by nanovoiding. Acta Mater 2012;60(13–14):5160–71. https://doi.org/10.1016/j.actamat.2012.06.014.
[18] Bhadeshia HKDH. Prevention of hydrogen embrittlement in steels. ISIJ Int 2016;56(1):24–36. https://doi.org/10.2355/isijinternational.isijint-2015-430.
[19] Sun B, Wang D, Lu X, Wan D, Ponge D, Zhang X. Current challenges and opportunities toward understanding hydrogen embrittlement mechanisms in advanced high-strength steels: a review. Acta Metall Sin 2021;34(6):741–54. https://doi.org/10.1007/s40195-021-01233-1.
[20] Depover T, den Eeckhout EV, Verbeken K. The hydrogen trapping ability of TiC and v4c3 by thermal desorption spectroscopy and permeation experiments. Procedia Struct Integr 2018;13:1414–20. https://doi.org/10.1016/j.prostr.2018.12.294.
[21] Li L, Song B, Cheng J, Yang Z, Cai Z. Effects of vanadium precipitates on hydrogen trapping efficiency and hydrogen induced cracking resistance in x80 pipeline steel. Int J Hydrogen Energy 2018;43(36):17353–63. https://doi.org/10.1016/j.ijhydene.2018.07.110.
[22] Pressouyre GM. A classification of hydrogen traps in steel. Metall Trans A 1979;10(10):1571–3. https://doi.org/10.1007/bf02812023.
[23] Pressouyre GM, Bernstein IM. A quantitative analysis of hydrogen trapping. Metall Trans A 1978;9(11):1571–80. https://doi.org/10.1007/bf02661939.
[24] Nagao A, Martin ML, Dadfarnia M, Sofronis P, Robertson IM. The effect of nanosized (ti, mo)c precipitates on hydrogen embrittlement of tempered lath martensitic steel. Acta Mater 2014;74:244–54. https://doi.org/10.1016/j.actamat.2014.04.051.
[25] Ramjaun TI, Ooi SW, Morana R, Bhadeshia HKDH. Designing steel to resist hydrogen embrittlement: Part 1 – trapping capacity. Mater Sci Technol 2018;34(14):1737–46. https://doi.org/10.1080/02670836.2018.1475919.
[26] dos Santos T, de Lima M, dos Santos D, Buono V. Effect of nano nb and v carbides on the hydrogen interaction in tempered martensitic steels. Int J Hydrogen Energy 2022;47(2):1358–70. https://doi.org/10.1016/j.ijhydene.2021.10.051.
[27] Stefano DD, Nazarov R, Hickel T, Neugebauer J, Mrovec M, Elsässer C. First-principles investigation of hydrogen interaction with TiC precipitates in α-fe. Phys Rev B May 2016;93(18). https://doi.org/10.1103/physrevb.93.184108.
[28] Nguyen J, Glandut N, Jaoul C, Lefort P. Hydrogen insertion in substoichiometric titanium carbide. Int J Hydrogen Energy 2015;40(27):8562–70. https://doi.org/10.1016/j.ijhydene.2015.05.009.
[29] Kamoutsi H, Haidemenopoulos G, Mavros H, Karantonidis C, Floratos P, Alhosani Z, Cho P, Anjum D, Ravaux F, Polychronopoulou K. Effect of precipitate coherency on the corrosion-induced hydrogen trapping in 2024 aluminum alloy. Int J Hydrogen Energy 2021;46(69):34487–97. https://doi.org/10.1016/j.ijhydene.2021.08.005.
[30] Fu Y, Li T, Yan Y-B, Wang X-Y, Zhu M-L, Xuan F-Z. A first principles study on h-atom interaction with bcc metals. Int J Hydrogen Energy 2023;48(26):9911–20. https://doi.org/10.1016/j.ijhydene.2022.11.275.
[31] Depover T, Verbeken K. The effect of TiC on the hydrogen induced ductility loss and trapping behavior of fe-c-ti alloys. Corrosion Sci 2016;112:308–26. https://doi.org/10.1016/j.corsci.2016.07.013.
[32] Depover T, Verbeken K. The detrimental effect of hydrogen at dislocations on the hydrogen embrittlement susceptibility of fe-c-x alloys: an experimental proof of the HELP mechanism. Int J Hydrogen Energy 2018;43(5):3050–61. https://doi.org/10.1016/j.ijhydene.2017.12.109.
[33] Wei FG, Tsuzaki K. Quantitative analysis on hydrogen trapping of TiC particles in steel. Metall Mater Trans 2006;37(2):331–53. https://doi.org/10.1007/s11661-006-0004-3.
[34] Dávila-Pérez MI, Reyes-Calderón F, Vázquez-Gómez O, Vergara-Hernández HJ, Villalobos JC, López-Martínez E. Hydrogen permeation in a cr–mo–v medium-carbon steel: effect of the quenching medium and tempering temperature. Int J Hydrogen Energy 2022;47(77):33105–11. https://doi.org/10.1016/j.ijhydene.2022.07.191.

[35] Vandewalle Liese, Cnockaert Vincent, Depover Tom, Verbeken Kim. The hydrogen trapping ability of Ti-based carbides in tempered martensitic steels evaluated by gaseous hydrogen charging at elevated temperature. In: Proceedings of the European corrosion congress (EUROCORR 2019); 2019. p. 8.
[36] Lee H, Lee J-Y. Hydrogen trapping by TiC particles in iron. Acta Metall 1984;32(1):131–6. https://doi.org/10.1016/0001-6160(84)90210-4.
[37] Wei F-G, Hara T, Tsuchida T, Tsuzaki K. Hydrogen trapping in quenched and tempered 0.42c-0.30ti steel containing bimodally dispersed TiC particles. ISIJ Int 2003;43(4):539–47. https://doi.org/10.2355/isijinternational.43.539.
[38] Vandewalle L, Depover T, Verbeken K. Hydrogen trapping of carbides during high temperature gaseous hydrogenation. Int J Hydrogen Energy 2023;48(82):32158–68. https://doi.org/10.1016/j.ijhydene.2023.04.348.
[39] Takahashi J, Kawakami K, Kobayashi Y, Tarui T. The first direct observation of hydrogen trapping sites in TiC precipitation-hardening steel through atom probe tomography. Scripta Mater 2010;63(3):261–4. https://doi.org/10.1016/j.scriptamat.2010.03.012.
[40] Chen Y-S, Haley D, Gerstl SSA, London AJ, Sweeney F, Wepf RA, Rainforth WM, Bagot PAJ, Moody MP. Direct observation of individual hydrogen atoms at trapping sites in a ferritic steel. Science 2017;355(6330):1196–9. https://doi.org/10.1126/science.aal2418.
[41] Takahashi J, Kawakami K, Tarui T. Direct observation of hydrogen-trapping sites in vanadium carbide precipitation steel by atom probe tomography. Scripta Mater 2012;67(2):213–6. https://doi.org/10.1016/j.scriptamat.2012.04.022.
[42] Takahashi J, Kawakami K, Kobayashi Y. Origin of hydrogen trapping site in vanadium carbide precipitation strengthening steel. Acta Mater 2018;153:193–204. https://doi.org/10.1016/j.actamat.2018.05.003.
[43] Chen Y-S, Lu H, Liang J, Rosenthal A, Liu H, Sneddon G, McCarroll I, Zhao Z, Li W, Guo A, Cairney JM. Observation of hydrogen trapping at dislocations, grain boundaries, and precipitates. Science 2020;367(6474):171–5. https://doi.org/10.1126/science.aaz0122.
[44] Huang S, Tian J, Liu Y. Atomic study of hydrogen behavior in different vanadium carbides. J Nucl Mater 2021;554:153096. https://doi.org/10.1016/j.jnucmat.2021.153096.
[45] Li Y, Zhang X, Wu T, Tang J, Deng L, Li W, Wang L, Deng H, Hu W. First-principles study on the dissolution and diffusion behavior of hydrogen in carbide precipitates. Int J Hydrogen Energy 2021;46(42):22030–9. https://doi.org/10.1016/j.ijhydene.2021.04.056.
[46] Liu Y, Huang S, Ding J, Yang Y, Zhao J. Vanadium carbide coating as hydrogen permeation barrier: a DFT study. Int J Hydrogen Energy 2019;44(12):6093–102. https://doi.org/10.1016/j.ijhydene.2019.01.049.
[47] Tang S, xian Li L, Peng Q, le Yan H, hui Cai M, ping Li J, yu Liu Z, dong Wang G. First-principles insights into hydrogen trapping in interstitial-vacancy complexes in vanadium carbide. Phys Chem Chem Phys 2022;24(34):20400–8. https://doi.org/10.1039/d2cp02425j.
[48] Ma Y, Shi Y, Wang H, Mi Z, Liu Z, Gao L, Yan Y, Su Y, Qiao L. A first-principles study on the hydrogen trap characteristics of coherent nano-precipitates in α-fe. Int J Hydrogen Energy 2020;45(51):27941–9. https://doi.org/10.1016/j.ijhydene.2020.07.123.
[49] Ding H, Fan X, Li C, Liu X, Jiang D, Wang C. First-principles study of hydrogen storage in non-stoichiometric TiCx. J Alloys Compd 2013;551:67–71. https://doi.org/10.1016/j.jallcom.2012.10.067.
[50] Salehin R, Thompson GB, Weinberger CR. Hydrogen trapping and storage in the group IVB-VIB transition metal carbides. Mater Des 2022;214:110399. https://doi.org/10.1016/j.matdes.2022.110399.
[51] Zhang B, Su J, Wang M, Liu Z, Yang Z, Militzer M, Chen H. Atomistic insight into hydrogen trapping at MC/BCC-fe phase boundaries: the role of local atomic environment. Acta Mater 2021;208:116744. https://doi.org/10.1016/j.actamat.2021.116744.
[52] Nazarov R, Hickel T, Neugebauer J. *Ab initio* study of h-vacancy interactions in fcc metals: implications for the formation of superabundant vacancies. Phys Rev B Apr. 2014;89(14). https://doi.org/10.1103/physrevb.89.144108.
[53] Korzhavyi PA, Pourovskii LV, Hugosson HW, Ruban AV, Johansson B. Ab initio study of phase equilibria in tic_x. Phys Rev Lett 2001;88:015505. https://doi.org/10.1103/PhysRevLett.88.015505.
[54] Hugosson HW, Korzhavyi P, Jansson U, Johansson B, Eriksson O. Phase stabilities and structural relaxations in substoichiometric tic_{1-x}. Phys Rev B 2001;63:165116. https://doi.org/10.1103/PhysRevB.63.165116.
[55] Goretzki H. Neutron diffraction studies on titanium-carbon and zirconium-carbon alloys. Phys Status Solidi 1967;20(2):K141–3. https://doi.org/10.1002/pssb.19670200260.
[56] Tsetseris L, Pantelides S. Vacancies, interstitials and their complexes in titanium carbide. Acta Mater 2008;56(12):2864–71. https://doi.org/10.1016/j.actamat.2008.02.020.
[57] Sun W, Ehteshami H, Korzhavyi PA. Structure and energy of point defects in TiC: an *ab initio* study. Phys Rev B Apr. 2015;91(13). https://doi.org/10.1103/physrevb.91.134111.
[58] Savin A, Nesper R, Wengert Steffen TF, Fässler Elf. The electron localization function. Angew Chem 1997;36:1808–32.
[59] Bader RFW. Atoms in molecules : a quantum theory. Oxford: Clarendon press; 1990.
[60] Henkelman G, Arnaldsson A, Jónsson H. A fast and robust algorithm for bader decomposition of charge density. Comput Mater Sci 2006;36(3):354–60. https://doi.org/10.1016/j.commatsci.2005.04.010.
[61] Yu M, Trinkle DR. Accurate and efficient algorithm for bader charge integration. J Chem Phys 2011;134(6):64111. https://doi.org/10.1063/1.3553716.
[62] Dronskowski R, Bloechl PE. Crystal orbital Hamilton populations (COHP): energy-resolved visualization of chemical bonding in solids based on density-functional calculations. J Phys Chem 1993;97(33):8617–24. https://doi.org/10.1021/j100135a014.
[63] Nelson R, Ertural C, George J, Deringer VL, Hautier G, Dronskowski R. Lobster: local orbital projections, atomic charges, and chemical-bonding analysis from projector-augmented-wave-based density-functional theory. J Comput Chem 2020;41(21):1931–40. https://doi.org/10.1002/jcc.26353.
[64] Maintz S, Deringer VL, Tchougréeff AL, Dronskowski R. Analytic projection from plane-wave and PAW wavefunctions and application to chemical-bonding analysis in solids. J Comput Chem 2013;34(29):2557–67. https://doi.org/10.1002/jcc.23424.
[65] Kresse G, Furthmüller J. Efficient iterative schemes for *ab initio* total-energy calculations using a plane-wave basis set. Phys Rev B 1996;54(16):11169–86. https://doi.org/10.1103/physrevb.54.11169.
[66] Perdew JP, Burke K, Ernzerhof M. Generalized gradient approximation made simple. Phys Rev Lett 1996;77(18):3865–8. https://doi.org/10.1103/physrevlett.77.3865.

[67] Kresse G, Joubert D. From ultrasoft pseudopotentials to the projector augmented-wave method. Phys Rev B 1999;59(3):1758–75. https://doi.org/10.1103/physrevb.59.1758.
[68] Monkhorst HJ, Pack JD. Special points for brillouin-zone integrations. Phys Rev B 1976;13(12):5188–92. https://doi.org/10.1103/physrevb.13.5188.
[69] Methfessel M, Paxton AT. High-precision sampling for brillouin-zone integration in metals. Phys Rev B 1989;40(6):3616–21. https://doi.org/10.1103/physrevb.40.3616.
[70] Henkelman G, Uberuaga BP, Jónsson H. A climbing image nudged elastic band method for finding saddle points and minimum energy paths. J Chem Phys 2000;113(22):9901–4. https://doi.org/10.1063/1.1329672.
[71] Sheppard D, Xiao P, Chemelewski W, Johnson DD, Henkelman G. A generalized solid-state nudged elastic band method. J Chem Phys 2012;136(7):074103. https://doi.org/10.1063/1.3684549.
[72] Paufler P, villars P, calvert l d. pearson's handbook of crystallographic data for intermetallic phases. Cryst Res Technol 1987;22(11):1436. https://doi.org/10.1002/crat.2170221117. american society for metals. metals park. ohio. 1986. vols. 1–3. 3258 pp, US $ 495.00 ISBN 0-87170-217-7.
[73] Nazarov R, Hickel T, Neugebauer J. First-principles study of the thermodynamics of hydrogen-vacancy interaction in fcc iron. Phys Rev B Dec. 2010;82(22). https://doi.org/10.1103/physrevb.82.224104.
[74] Epicier T, Acevedo D, Perez M. Crystallographic structure of vanadium carbide precipitates in a model fe-c-v steel. Phil Mag 2008;88(1):31–45. https://doi.org/10.1080/14786430701753816.
[75] Yazawa Y, Furuhara T, Maki T. Effect of matrix recrystallization on morphology, crystallography and coarsening behavior of vanadium carbide in austenite. Acta Mater 2004;52(12):3727–36. https://doi.org/10.1016/j.actamat.2004.04.027.
[76] Porter DA, Easterling K. Phase transformation in metals and alloys. New York, NY: springer; 1992.
[77] Rong W, Dunlop G. The crystallography of secondary carbide precipitation in high speed steel. Acta Metall 1984;32(10):1591–9. https://doi.org/10.1016/0001-6160(84)90218-9.
[78] Jung W-S, Lee S-C, Chung S-H. Energetics for interfaces between group IV transition metal carbides and bcc iron. ISIJ Int 2008;48(9):1280–4. https://doi.org/10.2355/isijinternational.48.1280.
[79] Hwu HH, Chen JG. Surface chemistry of transition metal carbides. Chem Rev 2004;105(1):185–212. https://doi.org/10.1021/cr0204606.
[80] Restrepo SE, Stefano DD, Mrovec M, Paxton AT. Density functional theory calculations of iron - vanadium carbide interfaces and the effect of hydrogen. Int J Hydrogen Energy 2020;45(3):2382–9. https://doi.org/10.1016/j.ijhydene.2019.11.102.
[81] Lee J-H, Shishidou T, Zhao Y-J, Freeman AJ, Olson GB. Strong interface adhesion in fe/TiC. Phil Mag 2005;85(31):3683–97. https://doi.org/10.1080/14786430500199278.
[82] Delft high performance computing centre (DHPC), DelftBlue supercomputer (phase 1). 2022. https://www.tudelft.nl/dhpc/ark:/44463/DelftBluePhase1.